VELOCITY FIELD OF A GENETIC ALGORITHM-BASED ACTIVELY CONTROLLED THREE-DIMENSIONAL TURBULENT WALL JET

Zachary M. Titus
Department of Mechanical Engineering
University of New Brunswick
15 Dineen Dr, Fredericton, New Brunswick, Canada
ztitus@unb.ca

Joseph W. Hall
Department of Mechanical Engineering
University of New Brunswick
15 Dineen Dr, Fredericton, New Brunswick, Canada
jwhall@unb.ca

ABSTRACT

An experimental study of an actively controlled three-dimensional round wall jet with sensor feedback at Re = 137 000 is presented. Unsteady wall pressure measurements were used in feedback to inform a genetic algorithm optimization of four independent inputs given to an array of synthetic jet actuators at the nozzle exit. The two-dimensional velocity field of the optimal control input half a nozzle diameter up from, and parallel to the wall, was measured using particle image velocimetry. The genetic algorithm control enhanced the lateral growth of the wall jet by up to 170% compared to the uncontrolled case, a significant improvement over previous control studies without feedback. Additionally, intermittent instances of bifurcation forced by the input were observed and are discussed in the current study.

INTRODUCTION

A three-dimensional round wall jet forms when fluid is issued from a circular nozzle and develops tangentially to a surface as depicted in Figure 1. A striking characteristic of the three-dimensional wall jet is its anisotropic growth, where the lateral growth rate is approximately 5.5 times larger than the vertical growth rate (Launder and Rodi, 1983). The growth is defined by lateral and vertical half-widths, which correspond to the points of half of the maximum mean streamwise velocity in the lateral and wall-normal shear-layers, respectively. The lateral and vertical half-widths, denoted by $z_{1/2}$ and $y_{1/2}$, respectively, are shown in Figure 1.

Perez et al. (2007) were the first to show that the disparity in growth of a three-dimensional round wall jet at Re = 28 500 could be enhanced with synthetic jet actuation. In this study, the lateral half-width was enhanced by 15%, while the vertical half-width was suppressed by 17% using a circumferential array of synthetic jet actuators impinging on the main jet at the nozzle exit at an angle of 45°. More recently, Ellis et al. (2025) showed that on a higher Reynolds number case at Re = 133 000, the lateral half-width could be increased by up to approximately 100% operating the synthetic jets at a Strouhal number, St, in the range $0.19 \leq St \leq 0.21$, and directly impinging on the main jet at the nozzle. Titus and Hall (2026) investigated the use of out-of-phase synthetic jet actuation directly impinging on the main jet at the nozzle with $St = 0.20$. Operating one half of the synthetic jet array 270° out of phase with the other was shown to have a significant impact, increasing the lateral half-width by 140% to the right of the jet centerline and 126% to the left.

Despite evidence of significant control authority in fully turbulent high Reynolds number wall jets, little attempt has been made to adapt wall jet control to the significant advancements made in the closely related controlled free jet. One example of modern advancement in free jet control, and the specific application in this study, is the use of evolutionary algorithms. This application uses heuristic operators to direct an actuation input toward an optimal outcome, such as optimized mixing in jets. In some cases, the use of evolutionary algorithms has revealed mechanisms behind the optimized control outcomes (Zhou et al., 2020). In a recent investigation, Titus and Hall (2025) applied a subclass of evolutionary algorithms, a genetic algorithm, to the controlled three-dimensional wall jet and showed that the magnitude of the wall pressure fluctuations could be enhanced with genetic algorithm-based feedback control. There, however, was no velocity data to determine the relationship between the unsteady wall pressure field and the velocity, the effect on the lateral growth, nor any investigation into the physics of the resulting control solutions. Each of these considerations is addressed in the current investigation with Particle Image Velocimetry (PIV) measurements of the two-dimensional velocity plane half a diameter up from, and parallel to the wall ($y/D = 0.5$) for the genetic algorithm-based control solution.

EXPERIMENT & METHODOLOGY

The experimental facility consists of a centrifugal blower that drives airflow through a settling chamber and a subsequent contoured nozzle of diameter D = 38.1 mm. The exit velocity is regulated at U_{exit} = 54.2 m/s, resulting in a Reynolds number Re = 137 000 based on the nozzle diameter and exit velocity. A 2.5m x 2.0m flat surface is placed tangential to the nozzle.

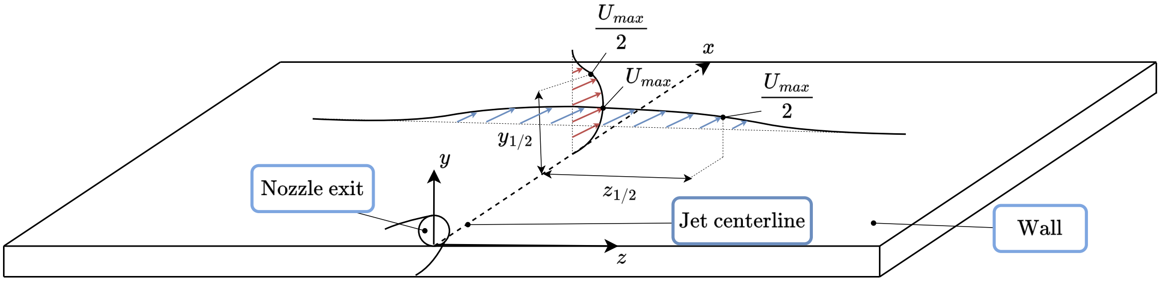

Figure 1: Schematic of the three-dimensional round wall jet.

At the nozzle, there are eight circumferentially mounted synthetic jet actuators impinging directly on the main jet as shown in Figure 2, which were designed to have a momentum coefficient $C_\mu = 0.013$. Alternating current (AC) voltage inputs are given to each of the synthetic jets, where each of the inputs has a fixed amplitude of 30V_{pp} and a frequency corresponding to a Strouhal number $St = 0.2$, as per the optimal conditions found in previous wall jet control studies (Ellis et al., 2025; Perez et al., 2007). The velocity field at $y/D = 0.5$ was measured using two-dimensional two-component PIV, and spanned 7.2 to 15 diameters downstream ($x/D = 7.2 - 15$). This plane was selected on the basis that it is considered a close approximation to the wall-normal distance containing the half-widths, y_{max}/D, before the far-field at $x/D = 20$. The flow was seeded with propylene glycol supplied by a Rosco Model 1900 Fog Machine, which has a mean particle diameter between 0.5-1.5 μm. A Quantel Evergreen Nd-YAG laser with a pulse energy of 200 mJ and wavelength of 532 nm was used. The camera used was a LaVision Imager CX-5, which is a CMOS sensor camera with a resolution of 2440 x 2040 and was equipped with a 28 mm lens and an optical bandpass filter. The timing between the camera and the laser pulses was achieved using a LaVision PTU X timing unit. The PIV images were captured 1.3 m above the wall with the camera mounted to a traverse.

Additionally, the unsteady wall pressure field was measured with time-resolved measurements using a spatial array of 89 electret condenser microphones spanning 5 to 15 diameters downstream ($x/D = 5 - 15$) and 4 diameters to the left and right of the jet centerline ($z/D = -4 - +4$). The microphones sense the flow via 1.5875 mm diameter pin holes and have a flat frequency response from 20 to 2000 Hz, which is sufficient to resolve the frequencies of interest in the flow.

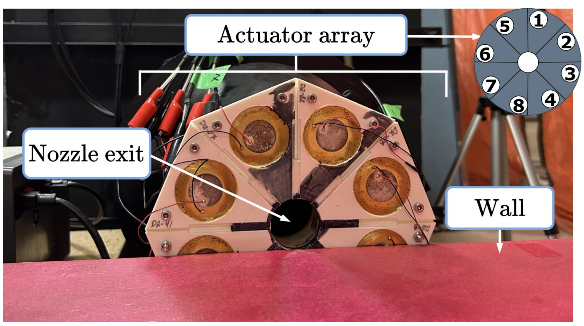

Figure 2: Experimental three-dimensional wall jet facility with synthetic jet actuator arrangement.

The primary experiment of this study consists of testing an actuation input $\mathbf{b} = [\phi_1, \phi_2, \phi_3, \phi_4]^T$, where an element b_i is a phase angle given to the pairs of synthetic jets labeled 1 and 2, 3 and 4, 5 and 6, and 7 and 8 in Figure 2, respectively. The input $\mathbf{b}$ is optimized using a genetic algorithm informed by unsteady wall pressure measurements in feedback measured by the condenser microphones. The resulting control solution, $\mathbf{b}$, determined from the genetic algorithm-based control, is then further explored with PIV measurements.

GENETIC ALGORITHM CONTROL RESULTS

It has been shown that the standard deviation in the wall pressure fluctuations off the jet centerline, where it is expected that the activity of large-scale structures is prominent, is correlated with lateral half-width enhancement. Out-of-phase actuation inputs with larger lateral half-widths result in larger standard deviations in wall pressure fluctuations off the jet centerline (Titus and Hall, 2026). This observation motivates the formalization of the genetic algorithm optimization objective, $C_{P_{RMS}}$, as,

$$\max \quad C_{P_{RMS}}(\mathbf{b}, \mathbf{s}) = \frac{\frac{1}{n}\sum_{i=1}^{n}\left[P_{RMS}(\mathbf{b}, s_i)_{ctr} - P_{RMS}(s_i)_{unctr}\right]}{\frac{1}{2}\rho U_{exit}^2} \tag{1}$$

where $\mathbf{s} = [s_1, s_2, ..., s_n]^T$ is the sensor subset of n separate microphones, the subscript i denotes the measurement from the i^{th} microphone, and P_{RMS} denotes the standard deviation in the wall pressure fluctuations of the i^{th} microphone. The subscripts ctr and $unctr$ refer to the synthetic jet-actuated and uncontrolled three-dimensional wall jet, respectively.

A brief description of the genetic algorithm approach used is given as follows. Upon initialization, N_{pop} number of candidate solutions, $\mathbf{b}$, are randomly generated, forming a 'population'. Each input is sent to the synthetic jets, where measurements from $\mathbf{s}$ are recorded, and a subsequent $C_{P_{RMS}}$ evaluation is made. After the evaluation of the initial population, the algorithm advances to the next iteration (termed 'generation') and evaluates a new set of N_{pop} control inputs. There are a total of N_{gen} generations. New generations are informed by genetic operators termed crossover, mutation, replication, and elitism. In elitism, the top N_e number of candidate control inputs are advanced directly to the next generation. In crossover, P_c% of the population goes through a process where partial solutions from two different control inputs are exchanged to form two new candidate solutions. In mutation, P_M% of the population goes through the process of selecting at random, one or multiple parameters from a candidate solution, and changing them. In replication, P_R% of the population is randomly selected to be transferred directly to the next generation. The selection process for control inputs that face genetic operators is informed by tournament selection, where N_t candidate solutions are selected at random, and the solution with the largest $C_{P_{RMS}}$ evaluation is selected for operators.

Multiple sets of genetic algorithm parameters were tested, and it was found that the set given in Table 1 resulted in the control input with the largest lateral growth. The parameter set favours local search of the objective function landscape, where the crossover parameter P_C is much larger than P_M. The imbalance between these two parameters tends to have the largest impact on the algorithm performance, and the crossover-favoured approach is typically used in flow control applications (Duriez et al., 2017).

Table 1: Genetic algorithm parameters.

N_{gen}	N_{pop}	P_M	P_C	P_R	N_e	N_t
20	50	20%	70%	6%	2	2

The convergence process of the optimization is illustrated in Figure 3 using proximity mapping. The method of proximity mapping is used to represent higher-dimensional vectors in two-dimensional space and has been used to interpret the evolution of control solutions in free jet control studies (Zhou et al. 2020). A variation on the traditional Multidimensional Scaling (MDS) used in proximity mapping, named landmark MDS (de Silva and Tenenbaum, 2004), is implemented to interpret the evolution of the control solution $\mathbf{b}$ relative to already-established control inputs. The referenced control inputs include $\mathbf{b} = [0°,\ 0°,\ 0°,\ 0°]^T$, $\mathbf{b} = [180°,\ 180°,\ 0°,\ 0°]^T$, and $\mathbf{b} = [270°,\ 270°,\ 0°,\ 0°]^T$ which are denoted by $\phi = 0°$, $\phi = 180°$, and $\phi = 270°$, respectively, and were investigated by Titus and Hall (2026). Additional helical inputs denoted by H_i are included in Figure 3. Helical control inputs are defined as inputs where each input to $\mathbf{b}$ is equally out-of-phase. H_1 through H_8 represents $\mathbf{b} = [0°,\ 90°,\ 270°,\ 180°]^T$, $\mathbf{b} = [270°,\ 0°,\ 180°,\ 90°]^T$, $\mathbf{b} = [90°,\ 180°,\ 0°,\ 270°]^T$, $\mathbf{b} = [280°,\ 270°,\ 90°,\ 0°]^T$, $\mathbf{b} = [0°,\ 270°,\ 90°,\ 180°]^T$, $\mathbf{b} = [90°,\ 0°,\ 180°,\ 270°]^T$, $\mathbf{b} = [270°,\ 180°,\ 0°,\ 90°]^T$, and $\mathbf{b} = [180°,\ 90°,\ 270°,\ 0°]^T$, respectively.

In landmark MDS, a set of feature vectors, $\boldsymbol{\gamma}_L = [\gamma_1,\ \gamma_2]^T$ is used to define each of the landmarks, which in this case are the reference control inputs, in two-dimensional space. These feature vectors are determined using the Euclidean distance matrix, whose elements are defined as,

$$d_{ij} = \left(\sum_{l=1}^{n} (\mathbf{b}_{i,l} - \mathbf{b}_{j,l})^2 \right)^{1/2} \tag{2}$$

where $n = 4$ is the dimension of the input vector $\mathbf{b}$, l denotes the element of $\mathbf{b}$, and d_{ij} denotes the Euclidean distance between the input vectors $\mathbf{b}_i$ and $\mathbf{b}_j$. A stress, σ, associated with the low-dimensional representation $\boldsymbol{\gamma}_L$ is given by,

$$\sigma = \sqrt{\frac{\sum (d_{ij} - \hat{d}_{ij})^2}{\sum d_{ij}^2}} \tag{3}$$

where $\hat{d}_{ij}$ denotes the elements of the Euclidean matrix associated with the low-dimensional representation $\boldsymbol{\gamma}_L$. A feature vector $\boldsymbol{\gamma}_L$ is then determined through gradient descent optimization such that σ is locally minimized. The feature vector $\boldsymbol{\gamma}_i^j$ associated with the i^{th} control input of generation j, $\mathbf{b}_i^j$, is determined by preserving the Euclidean distance between $\mathbf{b}_i^j$ and the landmark vectors in $\mathbb{R}^4$ using Equations 2 and 3. All control inputs reported in Figure 3 have $\sigma \leq 0.1$, which is considered a fair preservation of the relative distance between data points in the original dimension (Kruskal, 1964). With the use of landmark MDS, each control input needs only to preserve its relative distance between itself and the landmark points. Note that the magnitude of the coordinates γ_1 and γ_2 does not have any physical significance, only the relative distance between the feature vectors does, thus the magnitudes of γ_1 and γ_2 are omitted from Figure 3.

From the proximity mapping, the control inputs in the first reported generation, $j = 3$, are diverse and are generally associated with a relatively low $C_{P_{RMS}}$ value. As generations progress, the control inputs tend to cluster around certain points in the feature vector space. These points are associated with high $C_{P_{RMS}}$ values, and are representative of the stochastic genetic algorithm processes giving better-performing control solutions a higher probability of local search. As the generations progress up to $j = 15$, the convergence around a single control solution is apparent, and the candidate control solutions become less diverse. By $j = 15$, the algorithm is almost entirely converged on a single control input, with little diversity. The converged control input is $\mathbf{b} = [144.5°,\ 88.6°,\ 190.7°,\ 211.8°]^T$

VELOCITY FIELD RESULTS

The streamwise variation in lateral half-width from the genetic algorithm-discovered control input is compared alongside previously explored control inputs in Figure 4 (Titus and Hall, 2026). The compared actuation inputs $\mathbf{b} = [0°,\ 0°,\ 0°,\ 0°]^T$, $\mathbf{b} = [180°,\ 180°,\ 0°,\ 0°]^T$, and $\mathbf{b} = [270°,\ 270°,\ 0°,\ 0°]^T$, were found by simply varying the phase-angle of one half of the synthetic jet array. An impressive level of lateral growth enhancement is achieved for the genetic algorithm control input relative to the other inputs. The lateral half-width is increased by 173% to the right of the jet centerline and 152% to the left with respect to the uncontrolled case at the farthest reported streamwise position. This is an improvement over the results of Titus and Hall (2026), where the optimal forcing, $\mathbf{b} = [270°,\ 270°,\ 0°,\ 0°]^T$, yielded only a 140% increase to the right of the jet centerline and 126% to the left. These results further validate that actuation inputs with higher standard deviation in the wall pressure fluctuations away from the centerline result in a larger lateral growth. This is the first demonstration of using unsteady wall pressure measurements, which are, importantly, multi-point time-resolved measurements in feedback to enhance physical features of the wall jet in the velocity field. The resulting control solution, $\mathbf{b} = [144.5°,\ 88.6°,\ 190.7°,\ 211.8°]^T$, is unlikely to be found from combinatorial variation without sensor feedback and may excite new modes of wall jet development not achievable by simply tuning $\mathbf{b}$.

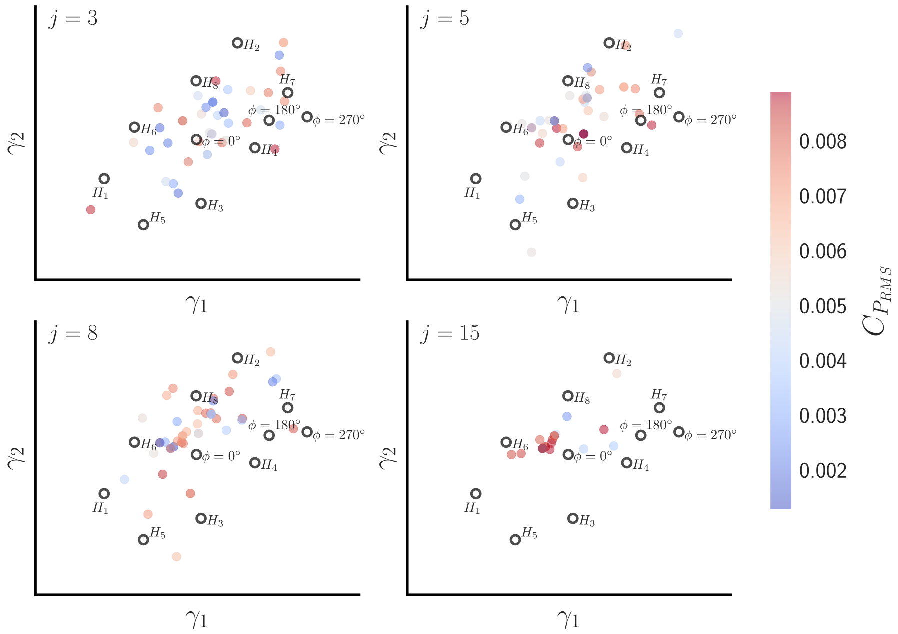

Figure 3: Proximity mapping of control solutions, **b**.

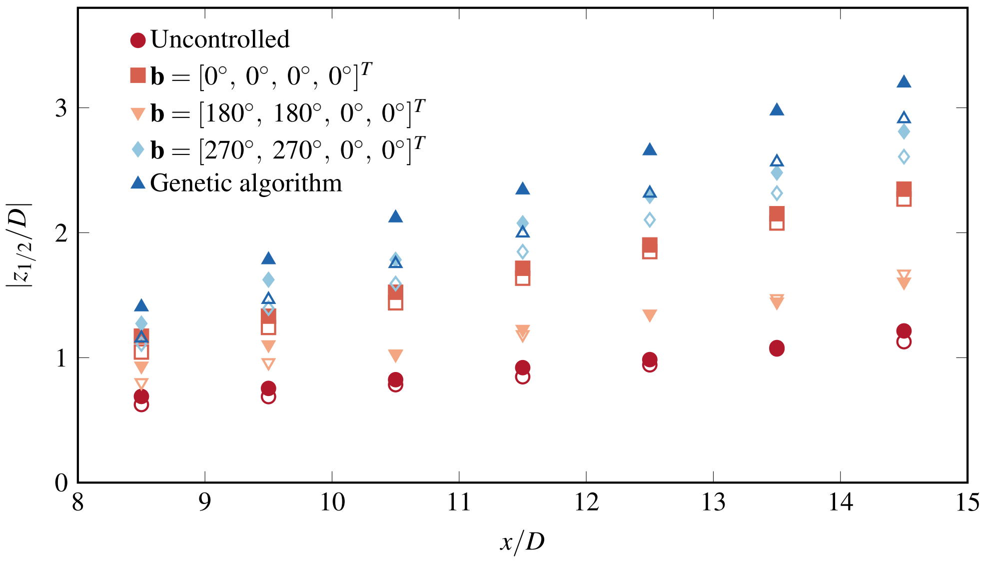

Figure 4: Streamwise variation in the lateral half-width to the right of the jet centerline (filled symbols - •, ■, ▼, ♦, ▲) and to the left of the jet centerline (open symbols - ◦, □, ▽, ◊, △) for various actuation inputs.

The mean streamwise velocity, U, normalized by the jet exit velocity, U_{exit}, for the uncontrolled wall jet and the genetic algorithm control case is shown in Figure 5a and 5b, respectively. The comparison of the two illustrates the stark difference in jet development forced by the genetic algorithm input. The mean streamwise velocity field is estimated from 2000 independent PIV images, resulting in an uncertainty $\varepsilon_U < 1.20\%$ measured at $z/D = \pm z_{1/2}/D$ based on the uncertainty in the estimation of a random variable formulated by George et al. (1978). For the genetic algorithm case, there is a significantly widened region of high mean streamwise velocity at $x/D < 8$, then the jet tapers and vectors towards the left, leaving a lobe-shaped region labeled A and forming a second lobe-shaped region B in Figure 5b. At $x/D \approx 9.5$, the region B tapers again toward a small peak denoted by region C, after which the jet continues to vector for the remainder of the development.

The mean lateral velocity field, W, normalized by the jet exit velocity, U_{exit}, for the genetic algorithm case is shown in Figure 6. The mean lateral velocity field displays organized regions of alternating sign across the jet centerline, annotated by the regions D, E, and F. Region D coincides with the first lobe shape noted in the mean streamwise velocity field. The center of regions E and F, which have strong negative and positive lateral velocities that cross the centerline, respectively, approximately coincide with the transitional changes in jet development denoted by regions B and C in Figure 5b. Past $x/D \approx 12$, the regions of competing mean lateral velocity become less apparent. The mean streamwise and lateral velocity fields suggest that the impact of the genetic algorithm control input is most influential on the development of the wall jet up to $x/D \approx 10-12$. The continued increase in lateral half-width beyond $x/D > 12$ in Figure 4 suggests that the impact of the control input on the development up to $x/D \approx 10-12$ affects the development into the intermediate-field.

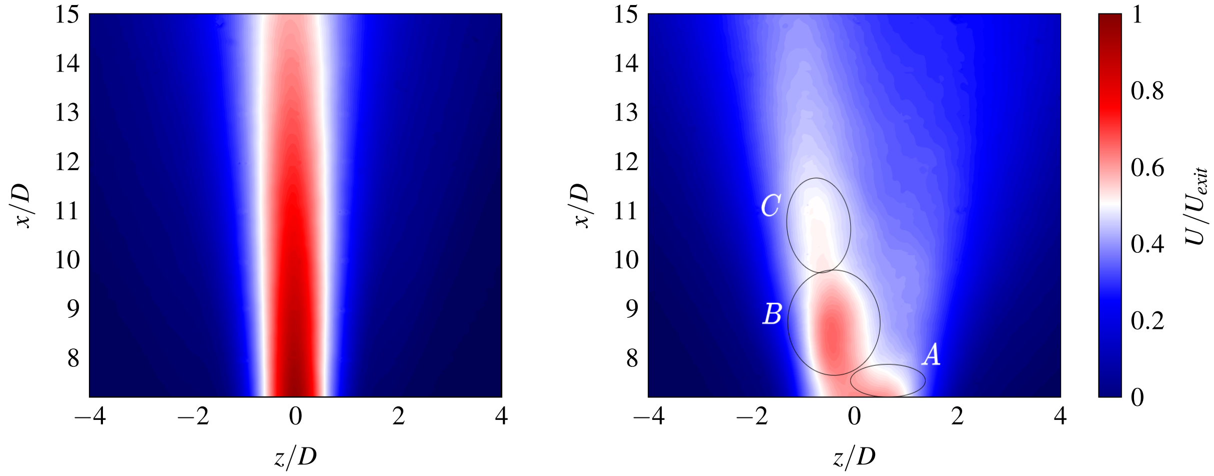

(a) (b)

Figure 5: Mean streamwise velocity field, (a) uncontrolled wall jet and (b) genetic algorithm control input.

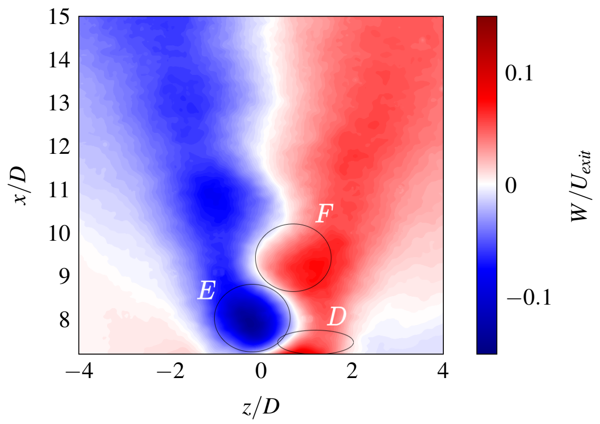

Figure 6: Mean lateral velocity field of the genetic algorithm control input.

It has been shown that the uncontrolled three-dimensional round wall jet development is primarily composed of intermittent instances of jet flapping and symmetric development (Sim and Hall, 2024). Titus and Hall (2026) showed that with basic configurations, $\mathbf{b} = [0°,\ 0°,\ 0°,\ 0°]^T$, $\mathbf{b} = [180°,\ 180°,\ 0°,\ 0°]^T$, and $\mathbf{b} = [270°,\ 270°,\ 0°,\ 0°]^T$, new modes of development were excited that enhance the lateral ejection of fluid. A significant distinguishing factor for the genetic algorithm control input is the frequent observation of bifurcation. Two instantaneous streamwise velocity fields illustrating this bifurcation, U_i, normalized by the jet exit velocity, U_{exit}, are given in Figure 7. The bifurcation label is inspired by the study of Reynolds et al. (2003), where a free jet was split into two streams (hence 'bifurcating') by using a combination of axial forcing upstream of the nozzle and helical forcing at the nozzle.

Figures 7a and 7b are annotated with the angled V-like shapes G and H to illustrate the separation of the jet into a stream on the left and right of the centerline. These instances are meant to present the two 'extremes' of the observed bifurcation. The organization and symmetry in the bifurcation of Figure 7a is of particular note and has been exclusively observed in the genetic algorithm control case. The instance shown in Figure 7b resembles an intermittent mode for the input $\mathbf{b} = [270°,\ 270°,\ 0°,\ 0°]^T$ noted by Titus and Hall (2026), where the jet vectors to the left and is accompanied by a significant lateral ejection of fluid to the right. Here, the jet develops into two streams at $x/D \approx 10$, however, the stream to the left appears to persist further downstream.

To further investigate the apparent bifurcation, a conditional average is applied to the set of 2000 PIV images. A subset of images is retained that agrees with the following conditions,

$$\frac{U_{i,(x,z)}}{U_{exit}} \leq \frac{0.8U_{(x,z)}}{U_{exit}},\ (x/D, z/D) = (13, 0)$$
$$\frac{U_{i,(x,z)}}{U_{exit}} \geq \frac{1.25U_{(x,z)}}{U_{exit}},\ (x/D,\ z/D) \in \left\{\begin{matrix}(8.5, 0.7),\\(9.5, 1.0),\\(10.5, 1.5)\end{matrix}\right\} \tag{4}$$

These conditions were selected such that each of the images exhibits the V-like separation, but the instances may vary in their organization and symmetry as noted in Figure 7. These conditions were met for 7% of the images.

The mean streamwise velocity field of the conditionally averaged PIV image subset is shown in Figure 8. The mean streamwise velocity field of the bifurcation instances shares similarities with the mean velocity field for the entire PIV image set shown in Figure 5b. Regions I, J, and K, labeled on Figure 8, share the same general development of regions A, B, and C in Figure 5b. The mean streamwise velocity field of the bifurcation instances, however, does exhibit the characteristic V-like shape indicative of bifurcation denoted by L in Figure 8, which is not apparent in Figure 5b. The bifurcation in the mean field is asymmetric, where the stream to the left is of higher velocity and persists further downstream relative to the stream on the right. The asymmetry indicates that bifurcation instances like that of Figure 7b likely make up the majority of the bifurcation image subset. Although the relatively organized and symmetric instances of bifurcation appear to be rarer, they illustrate the peak of control authority imposed by synthetic jet actuation on the wall jet achieved thus far. Further work should be done to research the nature of the organized bifurcation and attempt to increase the frequency of occurrence.

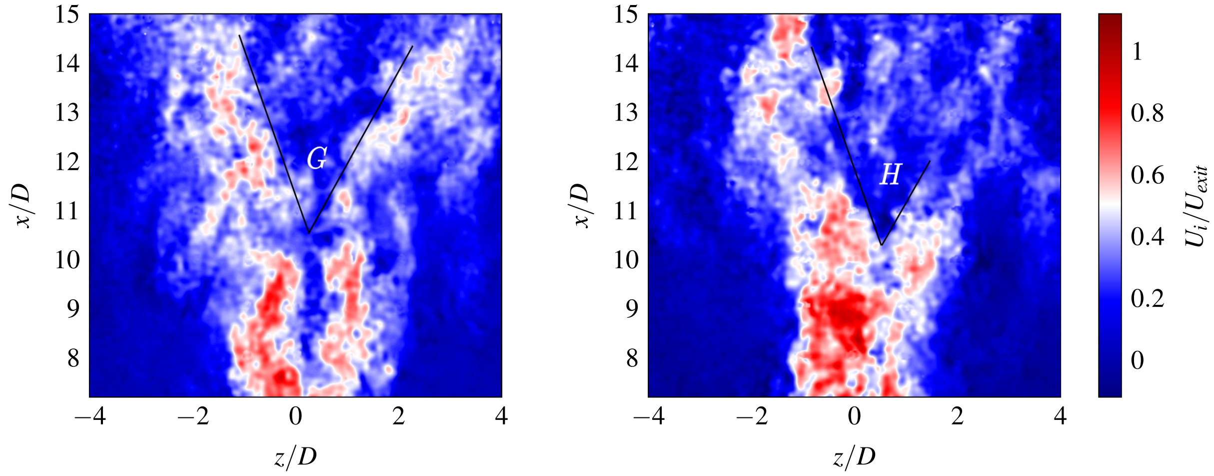

(a) (b)

Figure 7: Instances of bifurcation observed in the genetic algorithm control input, (a) organized bifurcation and (b) asymmetric bifurcation.

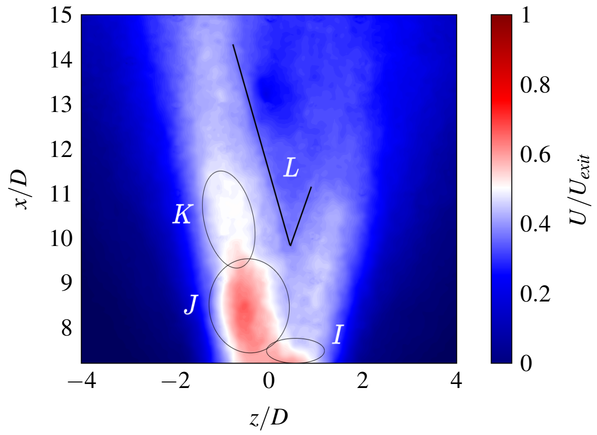

Figure 8: Mean streamwise velocity field of conditionally averaged bifurcation instances.

CONCLUSIONS

A synthetic jet-actuated three-dimensional wall jet controlled with genetic algorithm optimization and sensor feedback at Reynolds number $Re = 137\,000$ was experimentally investigated. Using this control approach, the lateral growth of the wall jet was enhanced by up to 170% compared to the uncontrolled development. This was the first demonstration of using the unsteady wall pressure field in feedback to enhance flow features of the wall jet in the velocity field. Intermittent instances of forced bifurcation in the wall jet were observed for the genetic algorithm control case. Among the 2000 PIV images, 7% met a defined bifurcation criterion. In some instances, the bifurcation was relatively symmetric and organized, and in other instances, the bifurcation was asymmetric where the stream to the left persisted further downstream. Future studies should continue to investigate the organized bifurcation instances. Stereoscopic PIV measurements would be valuable to determine if there are potential helical jet modes present. After further investigation of the bifurcation, an attempt to increase the frequency of occurrence or stabilize the wall jet on this mode would be of interest.

REFERENCES

Duriez, T., Brunton, S. L. & Noack, B. R. 2017 *Machine Learning Control – Taming Nonlinear Dynamics and Turbulence*, pp. 11–48. Springer.

Ellis, K. C., Sim, B. & Hall, J. W. 2025 The effect of axisymmetric nozzle forcing on turbulent three-dimensional wall jet development. In *AIAA SCITECH 2025 Forum*. AIAA 2025-1682.

George, W. K., Beuther, P. D. & Lumley, J. L. 1978 Processing of random signals. In *Proceedings of the Dynamic Flow Conference 1978 on Dynamic Measurements in Unsteady Flows*, , vol. 1, pp. 757–800.

Kruskal, J. B. 1964 Nonmetric multidimensional scaling: A numerical method. *Psychometrika* **29**, 115–129.

Launder, B. E. & Rodi, W. 1983 The turbulent wall jet-measurements and modelling. *Annual Review of Fluid Mechanics* **15**, 429–459.

Perez, C. L., Hall, J. W., Sagher, R. & Glauser, M. N. 2007 Towards controlling the three-dimensional wall jet development. In *37th AIAA Fluid Dynamics Conference and Exhibit*. AIAA 2007-4493.

Reynolds, W. C., Parekh, D. E., Juvet, P. J. D. & Lee, M. J. D. 2003 Bifurcating and blooming jets. *Annual Review of Fluid Mechanics* **35**, 295–315.

de Silva, V. & Tenenbaum, J. B. 2004 Sparse multidimensional scaling using landmark points. *Tech. Rep.* 41. Stanford.

Sim, B. & Hall, J. W. 2024 The velocity field parallel to the wall in a turbulent three-dimensional wall jet. In *Proceedings of the Thirteenth International Symposium on Turbulence and Shear Flow Phenomena*. Montreal, Canada.

Titus, Z. M. & Hall, J. W. 2025 Experimental closed-loop control of the three-dimensional turbulent wall jet using a genetic algorithm. In *AIAA SCITECH 2025 Forum*. AIAA 2025-1678.

Titus, Z. M. & Hall, J. W. 2026 Active control of a synthetic jet-actuated three-dimensional turbulent wall jet. *AIAA Journal.* (In press).

Zhou, Y., Fan, D., Zhang, B., Li, R. & Noack, B. R. 2020 Artificial intelligence control of a turbulent jet. *Journal of Fluid Mechanics* **897**, A27.